

Evolution of fractality in centrally concentrated young clusters

Almat Akhmetali^{1,2,*}, Adilkhan Assilkhan^{1,3,4,5}, Mordecai-Mark Mac Low⁴, Nurzhan Ussipov^{2,1}, Marat Zaidyn²,
Ernazar Abdikamalov^{1,6}, Alison Sills⁷, Xiaoying Pang^{8,9} and Bekdaulet Shukirgaliyev^{6,1,10,**}

¹ Energetic Cosmos Laboratory, Nazarbayev University, 53 Kabanbay Batyr Ave., Astana, 010000, Kazakhstan

² Department of Electronics and Astrophysics, Al-Farabi Kazakh National University, 71 Al-Farabi Ave., Almaty, 050040, Kazakhstan

³ Department of Astronomy, Columbia University, 538 W 120th St., New York, NY, 10027, USA

⁴ Department of Astrophysics, American Museum of Natural History, 200 Central Park W., New York, NY, 10024, USA

⁵ Gumarbek Daukeyev Almaty University of Power Engineering and Telecommunications, 126/1 Baytursynuli St., Almaty, 050000, Kazakhstan

⁶ Physics Department, Nazarbayev University, 53 Kabanbay Batyr Ave., Astana, 010000, Kazakhstan

⁷ Department of Physics and Astronomy, McMaster University, 1280 Main Street West Hamilton, ON, L8S 4M1, Canada

⁸ Department of Physics, Xi'an Jiaotong-Liverpool University, 111 Ren'ai Road, Dushu Lake Science and Education Innovation District, Suzhou 215123, Jiangsu Province, P.R. China

⁹ Shanghai Key Laboratory for Astrophysics, Shanghai Normal University, 100 Guilin Road, Shanghai 200234, PR China

¹⁰ Heriot-Watt University Aktobe Campus, K. Zhubanov Aktobe Regional University, 263 Zhubanov Brothers St., Aktobe, 030000, Kazakhstan

Received September XX, 20XX

ABSTRACT

We investigate the structural evolution of young star clusters forming within centrally concentrated molecular clouds. Our simulations use the Torch framework, which integrates the FLASH magnetohydrodynamics code with the AMUSE environment, enabling a self-consistent treatment of gas dynamics, star formation, stellar evolution, radiative transfer, and gravitational interactions. We quantify cluster structure using the Q parameter for fractality and compute fractal dimensions via two methods: box-counting and correlation dimension. Our results show that clusters generally inherit fractal substructure from their parental clouds, which is typically erased within $\sim 2.5 t_{\text{ff}}$ through dynamical relaxation. Massive stars can induce the formation of secondary subclusters via feedback, with outcomes strongly dependent on stellar mass and formation timing. Interactions among subclusters, including mergers and dispersal, can extend fractal structure beyond $4 t_{\text{ff}}$. We also find systematic correlations between the fractality parameter Q and the fractal dimension: fractality is positively correlated with both the correlation and box-counting dimensions, with the correlation dimension exhibiting a stronger correlation. These results demonstrate how stellar feedback and internal dynamics jointly shape the measurable fractal properties of embedded star clusters.

Key words. (Galaxy:) open clusters and associations: general – Stars: formation – Magnetohydrodynamics (MHD)

1. Introduction

Most stars are born within giant molecular clouds, assembling in groups that can range from a few dozen to millions of members, known as star clusters (see, e.g., Lada & Lada 2003; Portegies Zwart et al. 2010; Krause et al. 2020). Current models suggest that such clusters emerge through the global hierarchical collapse of the clouds (Vázquez-Semadeni et al. 2017; Grudić et al. 2018). As a cloud undergoes gravoturbulent collapse (Larson 1981), it fragments into dense, star-forming clumps, referred to as subclusters (Mac Low & Klessen 2004; McKee & Ostriker 2007). When gravitationally bound, these subclusters can merge over time and form a single, larger star cluster.

The dynamical evolution of star clusters is a complex process influenced by many factors. Both numerical simulations and observational studies suggest that clusters inherit a fractal spatial structure from their parental molecular clouds (Cartwright & Whitworth 2004; Clarke 2010; Sánchez & Alfaro 2009; André et al. 2010, 2014;

Kuhn et al. 2014; Jaehrig et al. 2015; Arzoumanian et al. 2019; Ballone et al. 2020). Over time, this initial fractality is gradually erased due to internal gravitational interactions and external influences. During this evolution, unbound clusters dissolve into the field, while bound clusters contract toward their centers, forming more radially concentrated distributions. However, this is only a general picture. The precise timescale over which clusters lose their initial fractal distribution and the factors that dominate this transformation are still not well understood.

Some young clusters (e.g., ρ Ophiuchus) exhibit centrally concentrated morphologies as early as 1 Myr, suggesting rapid dynamical evolution in certain environments (Cartwright & Whitworth 2004). Conversely, substructured morphologies have been detected in much older clusters. For example, Sánchez & Alfaro (2009) reported significant substructure in NGC 1513 and NGC 1641, both older than 100 Myr. Recent N-body simulations by Daffern-Powell & Parker (2020) further support the idea that, under specific conditions, clusters may develop a centrally condensed distribution within just a few million years. These contrasting findings highlight the diversity in cluster evolution pathways and underscore the need for more detailed studies of fractal structure of clusters.

* Corresponding authors: almat.akhmetali@nu.edu.kz

** bekdaulet.shukirgaliyev@nu.edu.kz

Fractality has been extensively studied in observed systems and pure N-body simulations (Cartwright & Whitworth 2004; de La Fuente Marcos & de La Fuente Marcos 2006; Maschberger et al. 2010; Sun et al. 2022; Ussipov et al. 2024; Qin et al. 2025; Coenda et al. 2025; Akhmetali 2026), yet only a limited number of works have addressed the fractal nature of star clusters forming in hydrodynamical simulations of collapsing turbulent molecular clouds. An early investigation was conducted by Schmeja & Klessen (2006), who applied the so-called Q parameter, first introduced by Cartwright & Whitworth (2004), to both observations of young embedded star clusters and smoothed-particle hydrodynamics (SPH) simulations from Schmeja & Klessen (2004). They found that the Q values obtained from simulations were comparable to those measured for real star clusters, and reported no significant correlation between the fractality of the sink particle distributions and the properties of the turbulent field imposed on the simulated collapsing molecular clouds. A similar study was presented by Maschberger et al. (2010), who examined two simulations with cloud masses of 10^3 and $10^4 M_\odot$, performed by Bonnell et al. (2003) and Bonnell et al. (2008), respectively. In both cases, the resulting sink particle clusters initially formed with low Q values (around 0.4 – 0.5), indicative of a high degree of substructure. In the lower-mass, gravitationally bound cluster, Q increased to values characteristic of a non-fractal distribution within a couple of free-fall times. In contrast, for the higher-mass, initially unbound cluster, Q remained nearly constant. These results support the view that star clusters forming hierarchically begin with a fractal configuration, which is gradually erased through mergers and relaxation processes.

Low Q values during the early stages of star formation were also reported by Girichidis et al. (2012), although their study considered much smaller, highly unstable clouds ($\sim 100 M_\odot$). They found a mild dependence of Q on both the initial density profile and the mode of turbulence in the collapsing cloud. In contrast, hydrodynamical simulations by Parker & Dale (2015) and Gavagnin et al. (2017) showed little effect of stellar feedback on Q . Ballone et al. (2020) simulated clusters with masses between 10^4 and $10^5 M_\odot$ and found all clusters remained fractal after two free-fall times. More recently, Laverde-Villarreal et al. (2025) reported that their clusters formed from clouds of 2×10^4 , 8×10^4 , and $3.2 \times 10^5 M_\odot$ lose their fractal structure after approximately 2.5 free-fall times. Overall, these studies indicate that Q generally evolves from low values, characteristic of a fractal structure, to higher values, reflecting a more uniform, non-fractal configuration.

In this paper, we explore the emergence of fractality in young clusters seeded within centrally concentrated molecular gas structures. Unlike previous models that often assume a pre-existing stellar distribution—primarily used to investigate the dynamical evolution of clusters following instantaneous gas expulsion (e.g., Shukirgaliyev et al. 2017, 2018, 2019a,b, 2021; Kalambay et al. 2022, 2025; Ussipov et al. 2024; Bissekenov et al. 2024a,b; Ishchenko et al. 2025; Weis et al. 2025)—our work analyzes the stellar birth process within a dynamic environment. To achieve this, we utilize the suite of combined magnetohydrodynamic and N-body simulations from Assilkhan et al. (2026), which captures the self-consistent formation of stars from a collapsing gas clump. This allows for a more realistic investigation of the early dynamical coupling between the stellar and gaseous components and its impact on the resulting fractal structure.

The rest of the paper is organized as follows: Section 2 describes the simulation dataset and the statistical methods used to

quantify fractality. Section 3 presents our analysis of the structural evolution, and Section 4 summarizes the main conclusions of the study.

2. Methods

2.1. Simulations of star cluster formation

The simulations used in this work are adopted from Assilkhan et al. (2026). They were performed with the Torch framework (Wall et al. 2019, 2020), which couples the FLASH magnetohydrodynamics code (Fryxell et al. 2000; Dubey et al. 2014) to the AMUSE environment (Zwart et al. 2009; Pelupessy et al. 2013; Zwart et al. 2013; Portegies Zwart et al. 2019). Stellar evolution is modeled with SeBa (Portegies Zwart & Verbunt 1996; Toonen et al. 2012), gravitational interactions are integrated using the fourth-order Hermite N-body solver ph4 (McMillan et al. 2012), and Multiples and Small N are used to regularize close binaries and few-body interactions that arise dynamically during the simulation (Hut et al. 1995; Portegies Zwart & McMillan 2018).

The initial conditions are based on the centrally concentrated cluster formation model of Shukirgaliyev et al. (2017), which itself builds on the star formation framework of Parmentier & Pfalzner (2013). In this framework, the initial gas density profile is taken to be equal to the total (stars + gas) density profile prior to the onset of star formation. As a result, the initial density distribution is nearly uniform in the central region and becomes increasingly steep toward larger radii, following an approximate power-law decline with an index of ~ 3.3 in the outer parts. The initial gas mass is set to $M_{\text{gas}} = 2513 M_\odot$. The cloud is initialized with a virial parameter of $\alpha_{\text{vir}} = 0.5$ and a temperature of 20 K. In the low-density outer regions, the minimum resolution corresponds to 32^3 grid cells, yielding a minimum cell size of $\Delta x_{\text{max}} = 0.429$ pc.

The refinement level n was varied from $n = 3$ to $n = 6$, corresponding to maximum effective resolutions between 64^3 and 512^3 cells. The minimum cell size Δx_{min} , sink accretion radius r_{sink} , and sink formation threshold ρ_{sink} were adjusted to properly resolve the local Jeans length. For the lowest-resolution case ($n = 3$), ten independent random realizations with different random seeds were performed to capture statistical variations in cluster formation arising from stochastic IMF sampling. Simulations are labeled as nXsY, where X denotes the refinement level and Y indicates the random seed. We explore 13 simulations of Assilkhan et al. (2026) named n3s1–10, n4s1, n5s1, and n6s1. The key numerical parameters for each simulation are summarized in Table 1. Further details can be found in Assilkhan et al. (2026).

Table 1: Initial physical parameters adopted in the simulations.

| Parameter | Value |
|------------------------------------------------------|----------------------|
| Gas mass, M_{gas} | $2513 M_\odot$ |
| Sphere radius, R_{sphere} | 5.5 pc |
| Plummer radius, a_* | 1.1 pc |
| Minimum number of cells, $\text{Cells}_{\text{min}}$ | 32^3 |
| Maximum cell size, Δx_{max} | 0.429 pc |
| Temperature, $T_{\text{cl}} = T_{\text{amb}}$ | 20 K |
| Virial parameter, α_{vir} | 0.5 |
| Vertical magnetic field, B_z | 3×10^{-6} G |

2.2. Fractality

To quantify the fractal structure of the simulated star clusters, we employ two commonly used metrics: the Q parameter (Cartwright & Whitworth 2004), which is likely the most popular method to quantify fractality, and the fractal dimension f_{dim} (Imre & Bogaert 2006). The Q parameter provides a measure of the cluster’s spatial structure by comparing the normalized mean edge length of the minimum spanning tree to the mean separation between stars. Values of $Q < 0.8$ indicate a hierarchically substructured (fractal) distribution, while $Q > 0.8$ corresponds to a more centrally concentrated, radially smooth cluster.

The fractal dimension f_{dim} quantifies the degree of clustering and substructure in the stellar distribution. Lower values of f_{dim} correspond to highly substructured, filamentary distributions, whereas higher values indicate a nearly uniform or centrally concentrated distribution (Qin et al. 2025).

For each simulated cluster, we compute Q and f_{dim} at different evolutionary stages to investigate how the initial substructure evolves during the collapse and early dynamical evolution. These metrics allow us to track the dissolution of initial fractality and the emergence of a more relaxed, centrally concentrated configuration.

2.2.1. Q parameter

The Q parameter is commonly employed in the analysis of both observational data and simulations (Schmeja & Klessen 2006; Bastian et al. 2009; Cartwright 2009; Sánchez & Alfaro 2009; Maschberger et al. 2010; Parker & Meyer 2012; Parker 2014; Parker & Dale 2015; Ballone et al. 2020; Laverde-Villarreal et al. 2025; Coenda et al. 2025). This parameter is defined using normalized quantities to standardize the calculation as

$$Q = \bar{m}/\bar{s}, \quad (1)$$

where \bar{m} is the normalized mean edge length of the minimum spanning tree, and \bar{s} is the normalized mean interparticle separation. The normalization for s is the characteristic cluster size r_{cl} , defined as the radius of a sphere in three dimensions (3D) or circle in two dimensions (2D) centered on the center of mass of the cluster and enclosing 95% of its total mass. Following Cartwright (2009), the minimum spanning tree mean edge length m is normalized by $(r_{\text{cl}}^2 N_s)^{1/2}$ in 2D, and by $(\frac{4}{3}\pi r_{\text{cl}}^3 N_s)^{1/3}$ in 3D, where N_s is the total number of stars.

Values of Q close to zero indicate that the mean MST edge length, \bar{m} , is much smaller than the mean interparticle separation, \bar{s} . This corresponds to a highly subclustered distribution, where points form tight, isolated groups with small \bar{m} separated by large distances \bar{s} . In contrast, higher Q values represent a smooth, uniform distribution in which \bar{m} and \bar{s} are comparable. Generally, values of Q below a threshold of 0.8 for 2D distributions, or 0.7 for 3D, indicate substructured morphologies, whereas values of Q above these thresholds correspond to smooth, centrally concentrated distributions. A Q value close to the threshold suggests an approximately uniform density profile.

2.2.2. Fractal dimension

Fractal dimension quantitatively characterizes the spatial arrangement of stars within a cluster. This metric reflects the degree of structural irregularity: lower fractal dimension values correspond to more clumpy and substructured morphologies,

while higher values indicate smoother, more centrally concentrated distributions (Qin et al. 2025). We calculate the fractal dimension using two different methods, box counting and neighbor counting.

The first method, box counting (Grassberger 1983), yields the Minkowski–Bouligand dimension (Imre & Bogaert 2006). This method involves covering the dataset with boxes of various sizes and counting how many are required to fully enclose the data for each size. Before applying this approach, the 3D and 2D coordinates of the stars are standardized to have zero mean and unit variance. This standardization ensures that the coordinates become dimensionless, and consequently, the box size L used in the calculation is also dimensionless. To reduce the influence of distant outliers, only stars located within a radius r_{cl} , defined as the radius enclosing 95% of the cluster’s mass around the cluster’s center of mass, are considered in the calculation.

The fractal dimension f_{dim} derived by the box-counting method is defined as

$$f_{\text{dim}} = -\frac{d \ln N(L)}{d \ln L}, \quad (2)$$

where L is the box size, and $N(L)$ is the number of boxes required to cover the spatial distribution of member stars for a given L . Since we are working with a finite set of discrete points, this derivative must be approximated using finite differences. Moreover, the estimated value of f_{dim} may vary with box size L . In our analysis, we estimate f_{dim} as the slope obtained through linear regression of $\ln N(L)$ versus $-\ln L$ (see Fig. 1(a)).

Figure 1(a) shows that plateaus appear when the number of boxes N approaches the total number of member stars. To reduce the bias introduced by these plateaus and to standardize the computation, we adopted a fixed fitting range of $[-\ln 2, \ln 2]$, marked by the vertical dashed lines in the figure. This interval corresponds to box sizes ranging from half to twice the characteristic scale set by the standard deviation of the coordinates, which approximately corresponds to the half-mass radius of the cluster.

The second method, neighbor-counting, computes the correlation integral (de La Fuente Marcos & de La Fuente Marcos 2006; Sánchez et al. 2007), approximated by the discrete sum

$$C(r) = \frac{1}{N_s(N_s - 1)} \sum_{i=1}^{N_s} n_i(r), \quad (3)$$

where $n_i(r)$ is the number of neighbors of the i -th star contained within a 3D sphere or 2D circle of radius r . As in the box-counting method, the coordinates were standardized to zero mean and unit variance prior to the calculation.

The number of neighboring stars $n_i(r)$ within a sphere of radius r centred on the i -th star is calculated as

$$n_i(r) = \sum_{\substack{j=1 \\ j \neq i}}^{N_s} \Theta(r - |\mathbf{x}_i - \mathbf{x}_j|), \quad (4)$$

where $\Theta(x)$ is the Heaviside step function, defined as $\Theta(x) = 0$ for $x < 0$ and $\Theta(x) = 1$ for $x \geq 0$ and $|\mathbf{x}_i - \mathbf{x}_j|$ is the distance between stars, which can be calculated in both 2D and 3D. In our analysis, f_{dim} is estimated as the slope obtained through linear regression of $\ln C(r)$ versus $\ln r$ (see Fig. 1(b)).

Figure 1(b) shows that a plateau develops when the average number of neighboring stars approaches the theoretical maximum, $N_s - 1$. The fitting ranges were therefore chosen to isolate

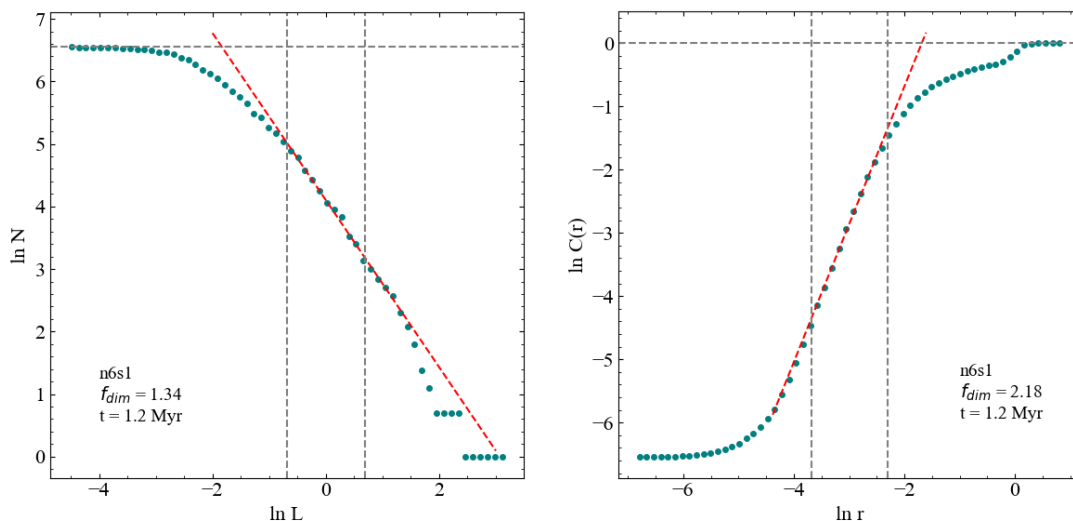


Fig. 1: *Left*: Box-counting dimension $\ln N(L)$ vs. $-\ln L$ for the *n6s1* model. The *red solid line* represents the best-fit linear regression, with its slope corresponding to the estimated fractal dimension f_{dim} . The vertical dashed lines mark the fitting range of $[-\ln 2, \ln 2]$. The horizontal *dashed line* indicates the natural logarithm of the total number of member stars in the cluster N_s . *Right*: Correlation dimension $\ln C(r)$ vs. $\ln r$ for the same model. The *red solid line* represents the best-fit linear regression, with its slope corresponding to the estimated fractal dimension f_{dim} . The vertical *dashed lines* mark the fitting range of $[-\ln 40, \ln 0.1]$. The horizontal *dashed line* indicates the natural logarithm of the normalized number of maximum neighbors, $\ln 1$.

the approximately linear regime of the $\ln C(r)$ – $\ln r$ relation prior to the onset of this saturation. Since the scale at which the plateau appears shifts to smaller r as the total number of stars increases, the extent of the linear regime depends on N_s . This occurs because, even after coordinate normalization, the mean interparticle separation decreases with increasing N_s , causing the correlation integral to reach saturation at smaller radii. Consequently, different fitting intervals were adopted: $[-\ln 10, \ln 0.5]$ for the *n3s1*–*n4s1* models, $[-\ln 20, \ln 0.2]$ for *n5s1*, and $[-\ln 40, \ln 0.1]$ for *n6s1*.

3. Results

Young clusters are generally thought to inherit their fractal structure from their parental molecular clouds, acquiring this property through the collapse of local clumps. Over time, dynamical interactions gradually erase this fractality. However, key questions remain: what factors drive the change in a cluster’s fractality, and on what timescale is it lost?

In this work, the term cluster refers to the full stellar population formed within the simulation volume at a given snapshot, whether or not gravitationally bound, while subclusters denote local overdensities within this population, regardless of whether they are gravitationally bound to the cluster potential.

3.1. Formation of subclusters

Models that form two or more distinct subclusters are presented in Figure 2, which shows the stellar distribution and gas density evolution for *n3s6*, *n3s7*, and *n4s1*. In *n3s6*, the first massive star is formed around 0.9 Myr, after which stellar feedback disperses the surrounding gas and displaces the dense region, allowing a second subcluster to form. In *n3s7*, two subclusters form around 0.9 Myr and start to merge into one, but then separate again around 2.1 Myr and form multiple subclusters. In *n4s1*, two subclusters form in close proximity at about 1.2 Myr, merge

into a single system, and later separate again and form multiple subclusters.

These models show two scenarios of subcluster formation. First, as in *n3s6*, a massive star forms in a single cluster and expels the surrounding gas. The expelled gas sweeps up a dense shell where star formation occurs subsequently, forming the second subcluster. Second, as in the case of *n3s7* and *n4s1*, two subclusters form in close proximity, and start to merge until after dynamical relaxation they separate again and form a multiple subcluster system.

3.2. Evolution of fractality

Figure 3 shows the evolution of the fractality parameter Q for models that show early fractal structure but eventually transition to more centrally concentrated states. For nearly all of these models, the critical point occurs at around $2.5 t_{\text{ff}}$, when both the 2D and 3D Q values exceed their respective thresholds for fractal structure. Within our set of simulations, the transition from fractal to centrally concentrated configurations consistently occurs at $\sim 2.5 t_{\text{ff}}$, independent of numerical resolution and early fractal structure. Since all models share the same global density profile and mean volume density, this suggests that the dissolution of fractal substructure is primarily regulated by the global free-fall timescale of the parent cloud rather than by the initial degree of fractality. A similar timescale was recently reported by Laverde-Villarreal et al. (2025), whose molecular clouds were an order of magnitude more massive than ours, suggesting that the loss of fractality may scale universally across different cloud masses. We note, however, that exploring different initial density profiles and mean densities will be required to assess whether this timescale truly remains invariant under more diverse initial conditions. Overall, these results indicate that fractal substructure typically dissolves on a timescale of a few free-fall times.

An important question is whether the formation of massive stars drives or modifies the dissolution of fractal substructure

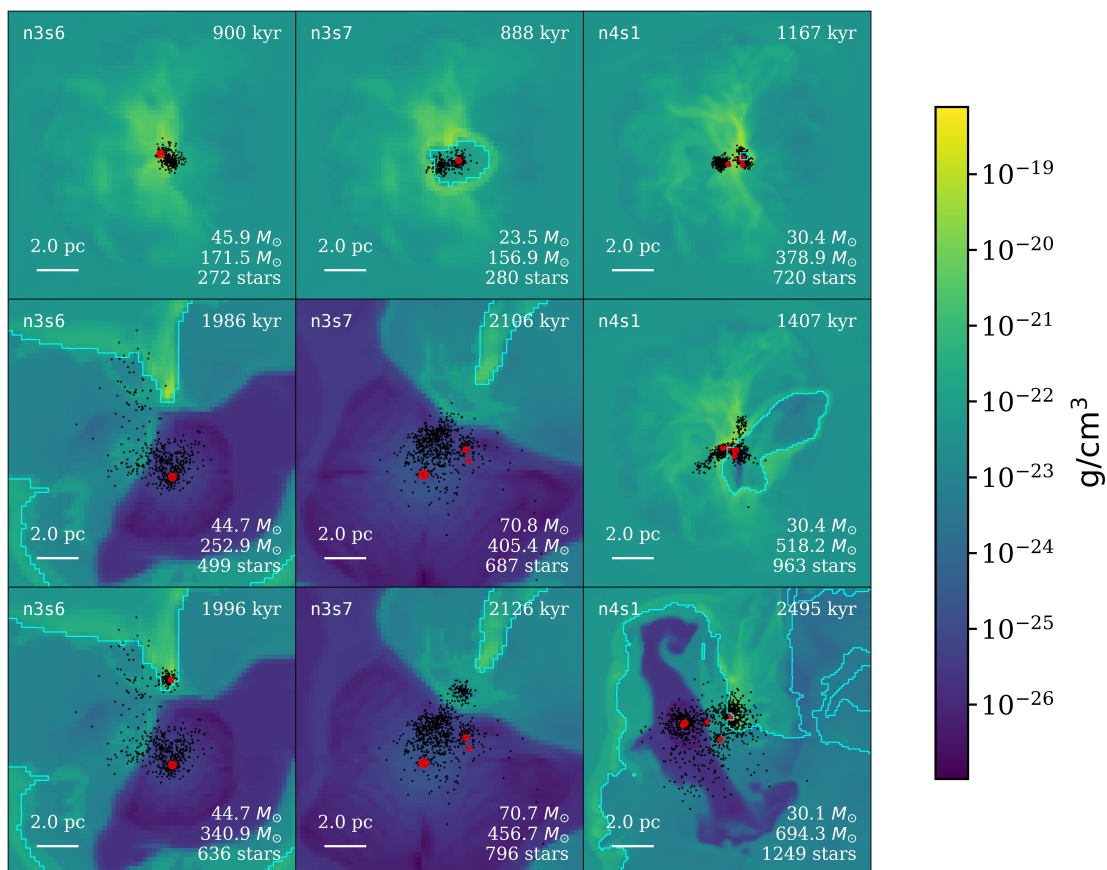


Fig. 2: Gas density slices and projected stellar distributions for the n3s6, n3s7, and n4s1 simulations, all of which exhibit subcluster formation. For n3s6 and n3s7: (*top row*) onset of stellar feedback; (*middle row*) just before the formation of the second subcluster; (*bottom row*) after its formation. For n4s1: (*top row*) two subclusters are present; (*middle row*) they merge into a single system; (*bottom row*) the system separates again into two subclusters. Ionization fronts are marked by cyan lines. Black dots indicate individual stars with $M < 7 M_{\odot}$, while massive stars ($M \geq 7 M_{\odot}$) are shown in red, with symbol sizes proportional to stellar mass. Annotations in each panel show: (*bottom left*) scale bar; (*bottom right*) mass of the most massive star, total stellar mass within 5.5 pc, and total number of stars; (*top left*) simulation label; and (*top right*) simulation time. The color scale indicates gas density in g cm^{-3} .

and the transition toward centrally concentrated stellar configurations. In some cases (e.g. n3s2, n3s5), the onset of massive star formation coincides with a sudden decrease in Q , consistent with feedback triggering secondary subclustering. However, this is not a universal outcome: in other models (n3s1, n3s8, n5s1) massive stars form without producing a measurable increase in fractality. Conversely, clusters such as n6s1 lose their substructure over time even in the absence of massive stars. While feedback can enhance subclustering in some environments, the global evolution of Q is governed by a combination of stellar feedback, dynamical relaxation, and the initial conditions of the parent cloud.

Figure 4 illustrates models that maintain fractality over longer timescales (snapshots of these models are shown in Figure 2). In these cases, Q remains below the fractality threshold even after $4 t_{\text{ff}}$, indicating the long-term survival of subclustering. Rather than converging toward a smooth, centrally concentrated structure, these systems preserve a dynamically evolving, hierarchical morphology. This behaviour is typically associated with the repeated formation, merging, and reorganization of subclusters driven by gravitational interactions and stellar feedback.

In particular, the fluctuations in Q observed for the n4s1 model are caused by the transient merging and subsequent separation of two nearby subclusters. When the subclusters temporarily

merge into a single system, the spatial distribution becomes more centrally concentrated and Q increases. As the system later re-fragments into multiple subclusters, the degree of substructure increases again, leading to a decrease in Q . These oscillations demonstrate that Q is sensitive not only to the presence of subclusters, but also to their dynamical interactions, making it an effective statistical tracer of time-dependent subclustering.

As demonstrated in Cartwright (2009), \bar{s} – \bar{m} plots provide an even more sensitive diagnostic of fractality. Figure 5 can be directly compared with Figures 1 and 2 in Cartwright (2009). Values indicate fractality if they lie below the dashed line corresponding to their dimensionality. At early times ($1 t_{\text{ff}}$ and $2 t_{\text{ff}}$), most 3D values of \bar{s} and \bar{m} fall within the region corresponding to fractal distributions with $f_{\text{dim}} \sim 2$ and 1.6. However, for the 2D projections, most clusters lie in ranges consistent with radial density profiles following $n \propto r^{\alpha}$ with slopes $\alpha \sim -2.5$ and -2 . By $3 t_{\text{ff}}$ and $4 t_{\text{ff}}$, both \bar{s} and \bar{m} decrease as the clusters evolve dynamically toward more centrally concentrated radial distributions. Consequently, the values of \bar{s} and \bar{m} converge toward those expected for radial density profiles with $\alpha \sim -2.9$ in both 2D and 3D cases, though three clusters continue to show clear fractal structure (n3s6, n3s7, and n4s1).

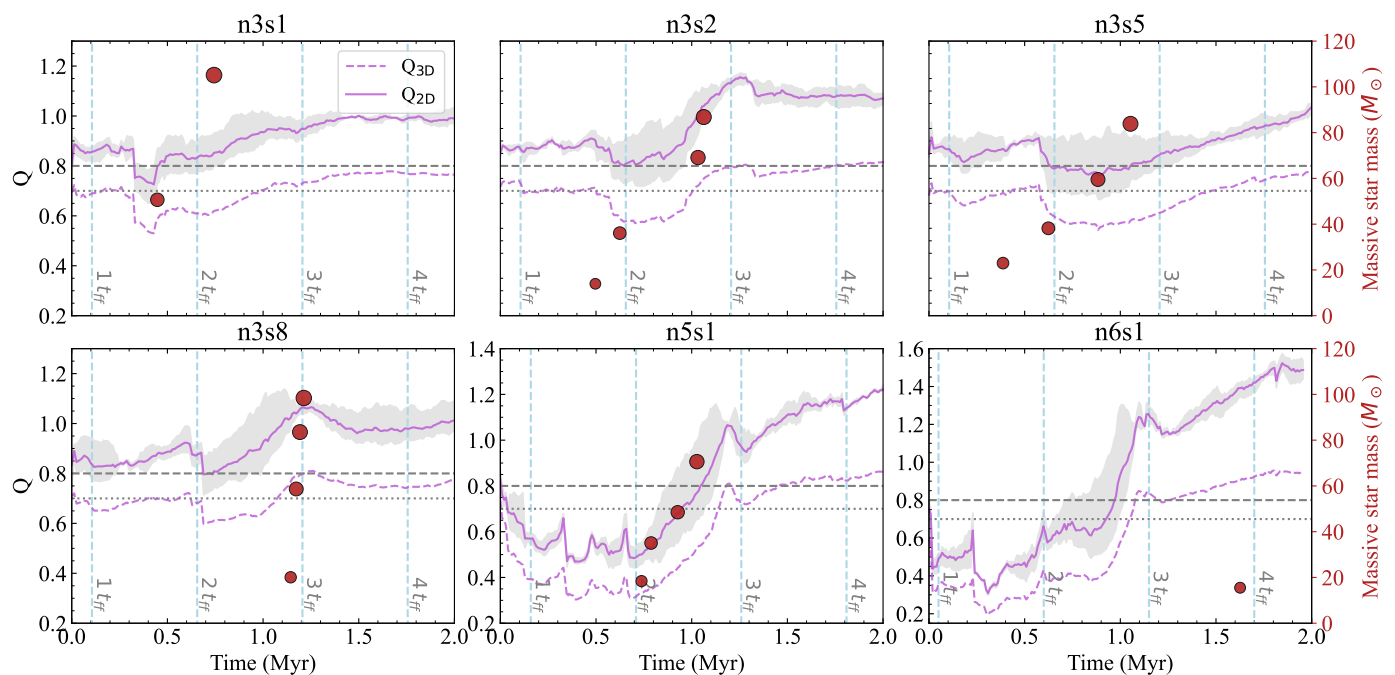


Fig. 3: Evolution of the Q parameter over time for models that initially exhibit fractality but subsequently evolve to smooth distributions. Time is measured starting from the onset of star formation. *Dashed purple lines* show the Q parameter calculated in 3D, while *solid purple lines* represent the mean Q values computed from 2D projections (xy , yz , and xz), with shaded areas indicating the minimum and maximum range of each projection. *Red circles* represent the mass and time of formation of massive stars, with marker size and vertical position proportional to their mass; the secondary *red y-axis* on the right indicates the mass scale of the massive stars. Vertical blue dashed lines denote multiples of the cloud’s free-fall time t_{ff} and *horizontal gray lines* mark the fractality thresholds for the Q parameter: 0.8 for 2D (*dashed line*) and 0.7 for 3D (*dotted line*) clusters.

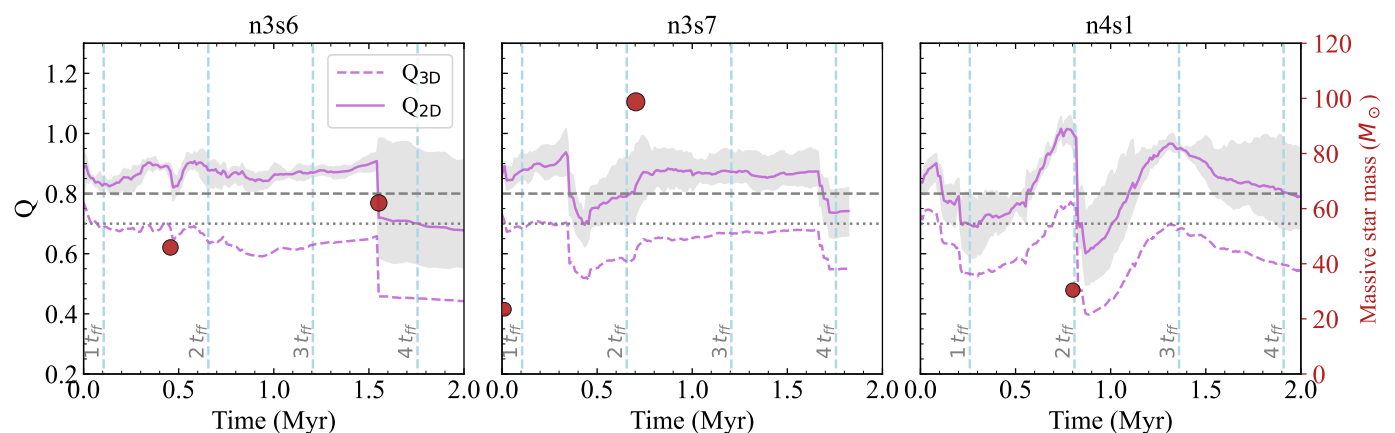


Fig. 4: Evolution of the Q parameter over time in models where subcluster formation maintained fractality after $4 t_{\text{ff}}$. All notation is the same as Figure 3.

3.3. Evolution of fractal dimension

Figure 6 shows the evolution of f_{dim} for the models that initially exhibit fractal structure as evaluated by low Q values but later lose it, as shown in Figure 3. In all models, f_{dim} increases sharply before $1 t_{\text{ff}}$, as expected, since star formation proceeds rapidly while the clusters are still assembling and gaining structural complexity. Two distinct behaviors can be identified. First, the $n3s^*$ models all show similar evolution. In these models, the correlation dimension in 3D $D_{\text{CD},3\text{D}}$ rises and reaches a plateau at approximately 2.4, while the box-counting dimension $D_{\text{BC},3\text{D}}$ stabilizes at about 1.8–1.9. In the 2D calculations, however,

both methods give very similar results, with both $D_{\text{CD},2\text{D}}$ and $D_{\text{BC},2\text{D}}$ converging to values around 1.5–1.6. Second, the higher-resolution models $n5s1$ and $n6s1$ show somewhat different behavior, particularly after $3 t_{\text{ff}}$. In these models, the box-counting dimension evolves similarly to the $n3s^*$ models but reaches a slightly lower plateau at about 1.3–1.4. In contrast, the correlation dimension continues to increase and exceeds 2.5 in 3D, while the corresponding 2D values remain within the same range as the other models.

The different behavior of the high-resolution models $n5s1$ and $n6s1$ is consistent with their large Q -parameter values ($Q \approx 1.2$), which indicate strongly centrally concentrated clusters with

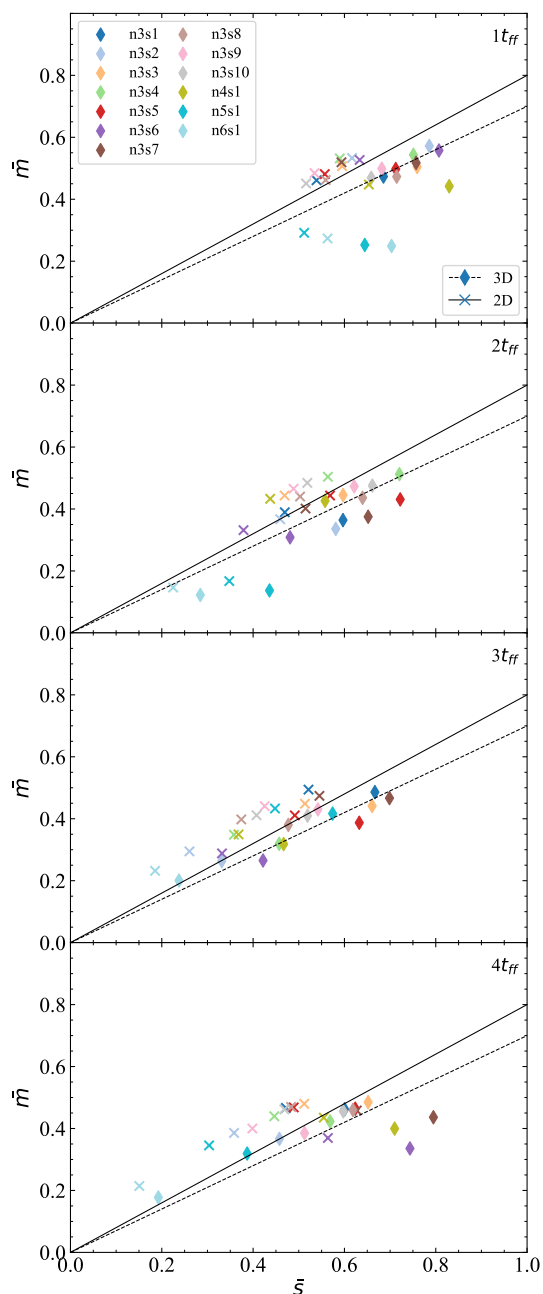


Fig. 5: Mean interparticle distance \bar{s} versus mean minimum spanning tree edge length \bar{m} (see Section 2.2.1) for all simulations at different multiples of the free-fall time t_{ff} , indicated in the upper right corner. *Diamonds and dashed lines* represent 3D results, while *cross markers with solid lines* represent mean values of 2D projections (xy , yz , and xz). Fractality is indicated by points lying below and to the right of the critical lines.

a radial density profile rather than a fractal structure. In such configurations, stars become densely packed toward the cluster center, significantly increasing the number of stellar pairs at small separations. Since the correlation dimension is based on pair statistics, this leads to a steeper correlation sum and consequently larger derived values of f_{dim} in 3D. In contrast, the box-counting dimension primarily reflects the global spatial extent of the cluster and is therefore less sensitive to strong central concentration, resulting in similar plateau values to those of

the lower-resolution models. In projection, these differences are partially suppressed, which explains why the corresponding 2D estimates remain comparable across all simulations.

Fig. 7 presents the evolution of f_{dim} over time for models that maintain their fractality as evaluated by low Q values throughout the simulation (see Fig. 4). In these models, f_{dim} increases during the first free-fall time and, after some fluctuations, plateaus at approximately 1.4–1.5, similar to Figure 6. However, a clear correlation is observed between sudden drops in Q (Fig. 4) and increases in f_{dim} around $1.5 t_{\text{ff}}$ and $2 t_{\text{ff}}$ for n3s7 and n4s1, respectively. These sharp decreases in Q and corresponding increases in f_{dim} coincide with the formation of the second subclusters in these models (Fig. 2, middle and right columns).

3.4. Correlation of fractality and fractal dimension

The Q parameter indicates whether a system is fractal, whereas f_{dim} quantifies the degree of fractality. However, there is no widely accepted or consistent correlation between them, especially when comparing Q with f_{dim} estimated using different methods. In this section, we examine the possible correlations between Q and f_{dim} obtained from the box-counting method and the correlation sum.

Figure 8 shows the dependence of f_{dim} on Q parameter. We consider only snapshots with $Q < 0.7$, corresponding to fractal distributions. In the left panel, the points represent mean values with error bars showing the standard deviation. The correlation between the two variables was quantified with Spearman’s rank correlation coefficient ρ (Zwillinger & Kokoska 1999). By definition, $\rho = +1$ corresponds to a perfect positive correlation, $\rho = 0$ to no correlation, and $\rho = -1$ to a perfect negative correlation. We find that Q shows a weak positive correlation with the box-counting dimension and a moderate positive correlation with the correlation dimension. This is in tension with the findings of Sánchez & Alfaro (2009), who found strong correlation between fractality and fractal dimension when applied to artificial clusters.

The accuracy of f_{dim} estimation depends critically on the number of points considered, with larger N_{thr} reducing uncertainties. We limit our analysis to snapshots with $N_{\text{thr}} \leq 500$, since for larger N_{thr} the number of available snapshots decreases, preventing statistically robust conclusions. The right panel of Figure 8 shows the Spearman rank correlation coefficient ρ as a function of the minimum number of stars per snapshot N_{thr} . We find the positive correlation between f_{dim} and Q remains stable across the considered range.

The correlation dimension exhibits a stronger correlation with Q than the box-counting dimension because it is more sensitive to the local clustering of stars and captures the scaling behavior of inter-point distances. In contrast, the box-counting dimension provides a more global measure of the overall spatial extent of the distribution, making it less responsive to local substructure. As a result, variations in Q , which primarily reflect changes in local clumpiness, are more directly reflected in the correlation dimension than in the box-counting dimension.

4. Conclusions

In this study, we investigated the evolution of fractality in centrally concentrated young star clusters and the role of massive stars in subcluster formation. Using a set of simulations of cluster formation from gas with different realizations of our initial conditions and numerical resolutions, we followed the gas collapse, star formation, and cluster assembly processes to analyze

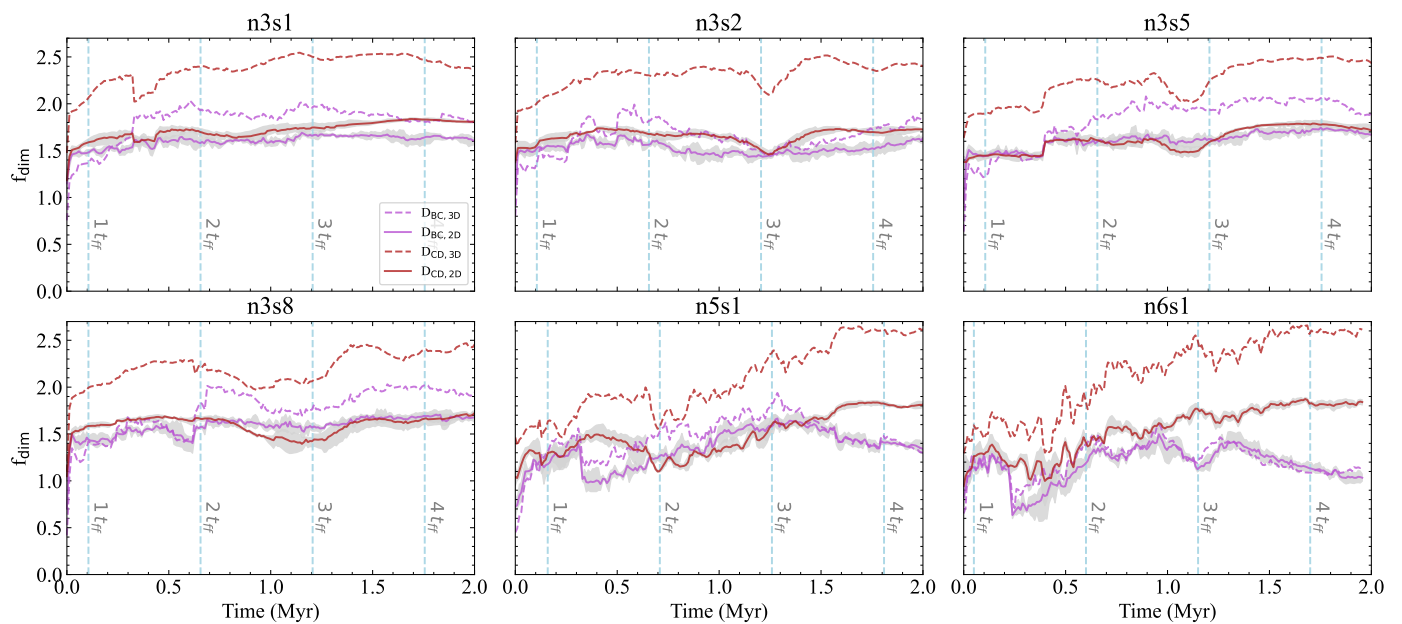


Fig. 6: Evolution of the fractal dimension f_{dim} over time for the models that initially exhibit fractality but subsequently lose it shown in Figure 3. Both the box counting dimension D_{BC} (purple lines) and correlation dimension D_{CD} (brick red lines) are shown. Time is measured starting from the onset of star formation. Dashed lines show f_{dim} calculated in 3D, while solid lines represent the mean f_{dim} values computed from 2D projections (xy , yz , and xz), with shaded areas indicating the minimum and maximum range of each projection. Vertical blue dashed lines denote multiples of the cloud’s free-fall time t_{ff} .

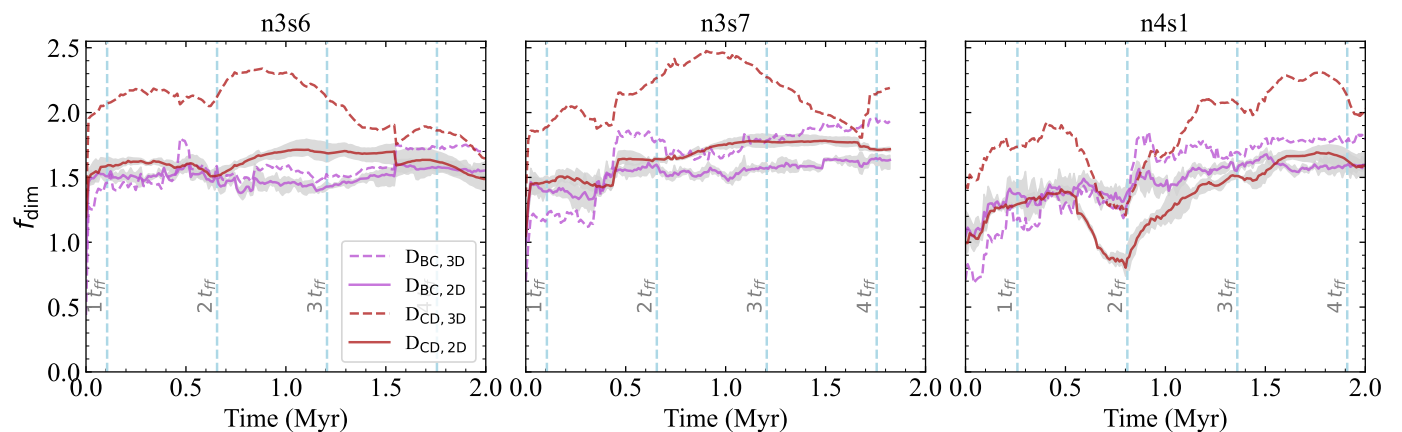


Fig. 7: Evolution of the fractal dimension f_{dim} over time in models where the formation of subclusters allowed fractality as evaluated by low Q values to be maintained even after $4 t_{\text{ff}}$ (see Fig. 4). All notations are the same as in Figure 6.

how these factors influence fractal structure and cluster concentration. We find the following conclusions.

- Young clusters inherit fractal substructure from their parental molecular clouds, but in most cases this pattern is erased by dynamical relaxation at about $\sim 2.5 t_{\text{ff}}$, regardless of the simulation resolution.
- Feedback from massive stars can trigger the formation of secondary subclusters, but its impact is not universal: whether feedback enhances fractality depends on both the stellar mass of stars producing significant feedback and the location and timing of their formation.
- Interactions among subclusters, including their formation, merging, and dispersal, can sustain measurable fractality beyond $4 t_{\text{ff}}$.
- In the highest-resolution models (n5s1 and n6s1), which evolve toward strongly centrally concentrated clusters ($Q \sim$

1.2), the correlation dimension increases further in 3D while the box-counting dimension remains nearly constant, reflecting the higher sensitivity of the correlation dimension to dense stellar cores.

- The Q parameter shows weak positive correlation with box-counting dimension, and moderate positive correlation with correlation dimension.

Acknowledgements. This research was funded by the Science Committee of the Ministry of Science and Higher Education of the Republic of Kazakhstan (Grant No. AP26103591). AA acknowledges support from a Bolashaq International Scholarship. EA is partially supported by Nazarbayev University Faculty Development Competitive Research Grant Program (no. 040225FD4713). M-MML is partially supported by US National Science Foundation grant AST23-07950. XP acknowledges the financial support of the National Natural Science Foundation of China through grants 12573036, 12233013 and the China Manned Space Program with grant No. CMS-CSST-2025-A08.

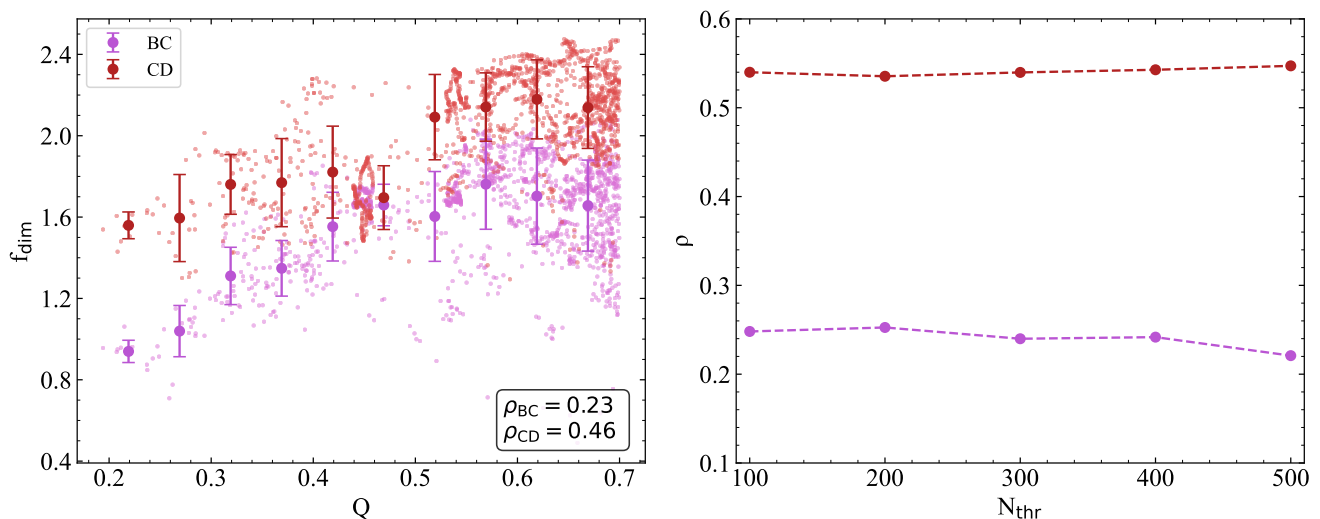


Fig. 8: Correlation between the fractal dimension f_{dim} and the Q parameter for the 3D stellar distributions. *Left panel:* binned mean values of f_{dim} as a function of Q for snapshots with $Q < 0.7$. The box-counting dimension is shown in *purple* and the correlation dimension in *red*, with error bars indicating the standard deviation within each bin. Spearman's rank correlation coefficient ρ is shown for each dimension in the legend. *Right panel:* variation of ρ as a function of the threshold number of stars per snapshot (N_{thr}).

References

- Akhmetali, A. 2026, *Journal of Astrophysics and Astronomy*, 47, 4
- André, P., Di Francesco, J., Ward-Thompson, D., et al. 2014, *Protostars and planets VI*, 27
- André, P., Men'shchikov, A., Bontemps, S., et al. 2010, *Astronomy & Astrophysics*, 518, L102
- Arzoumanian, D., André, P., Könyves, V., et al. 2019, *Astronomy & Astrophysics*, 621, A42
- Assilkhan, A., Mac Low, M.-M., Polak, B., et al. 2026, *A&A*, 705, A79
- Ballone, A., Mapelli, M., Di Carlo, U. N., et al. 2020, *Monthly Notices of the Royal Astronomical Society*, 496, 49
- Bastian, N., Gieles, M., Ercolano, B., & Gutermuth, R. 2009, *Monthly Notices of the Royal Astronomical Society*, 392, 868
- Bissekenov, A., Kalambay, M., Abdikamalov, E., et al. 2024a, *A&A*, 689, A282
- Bissekenov, A., Kalambay, M. T., Abylkairov, Y. S., & Shukirgaliyev, B. T. 2024b, *Recent Contributions to Physics*, 90
- Bonnell, I. A., Bate, M. R., & Vine, S. G. 2003, *Monthly Notices of the Royal Astronomical Society*, 343, 413
- Bonnell, I. A., Clark, P., & Bate, M. R. 2008, *Monthly Notices of the Royal Astronomical Society*, 389, 1556
- Cartwright, A. 2009, *Monthly Notices of the Royal Astronomical Society*, 400, 1427
- Cartwright, A. & Whitworth, A. P. 2004, *Monthly Notices of the Royal Astronomical Society*, 348, 589
- Clarke, C. 2010, *Philosophical Transactions of the Royal Society A: Mathematical, Physical and Engineering Sciences*, 368, 733
- Coenda, V., Baume, G., Palma, T., & Feinstein, C. 2025, *Astronomy & Astrophysics*, 699, A15
- Daffern-Powell, E. C. & Parker, R. J. 2020, *Monthly Notices of the Royal Astronomical Society*, 493, 4925
- de La Fuente Marcos, R. & de La Fuente Marcos, C. 2006, *Astronomy & Astrophysics*, 452, 163
- Dubey, A., Antypas, K., Calder, A. C., et al. 2014, *The International journal of high performance computing applications*, 28, 225
- Fryxell, B., Olson, K., Ricker, P., et al. 2000, *The Astrophysical Journal Supplement Series*, 131, 273
- Gavagnin, E., Bleuler, A., Rosdahl, J., & Teyssier, R. 2017, *Monthly Notices of the Royal Astronomical Society*, 472, 4155
- Girichidis, P., Federrath, C., Allison, R., Banerjee, R., & Klessen, R. S. 2012, *Monthly Notices of the Royal Astronomical Society*, 420, 3264
- Grassberger, P. 1983, *Physics Letters A*, 97, 224
- Grudić, M. Y., Guszejnov, D., Hopkins, P. F., et al. 2018, *Monthly Notices of the Royal Astronomical Society*, 481, 688
- Hut, P., Makino, J., & McMillan, S. 1995, *Astrophysical Journal, Part 2-Letters (ISSN 0004-637X)*, vol. 443, no. 2, p. L93-L96, 443, L93
- Imre, A. R. & Bogaert, J. 2006, *Fractals*, 14, 49
- Ishchenko, M., Masliukh, V., Hradov, M., et al. 2025, *A&A*, 694, A33
- Jaehnig, K. O., Da Rio, N., & Tan, J. C. 2015, *The Astrophysical Journal*, 798, 126
- Kalambay, M. T., Naurzabayeva, A. Z., Otebay, A. B., et al. 2022, *Recent Contributions to Physics*, 83, 4
- Kalambay, M. T., Otebay, A. B., Nazar, A. B., Assilkhan, A., & Shukirgaliyev, B. T. 2025, *Herald of the Kazakh-British Technical University*, 22, 312
- Krause, M. G., Offner, S. S., Charbonnel, C., et al. 2020, *Space Science Reviews*, 216, 64
- Kuhn, M. A., Feigelson, E. D., Getman, K. V., et al. 2014, *The Astrophysical Journal*, 787, 107
- Lada, C. J. & Lada, E. A. 2003, *Annual Review of Astronomy and Astrophysics*, 41, 57
- Larson, R. B. 1981, *Monthly Notices of the Royal Astronomical Society*, 194, 809
- Laverde-Villarreal, E., Sills, A., Courmoyer-Cloutier, C., & Arias Callejas, V. 2025, *The Astrophysical Journal*, 989, 22
- Mac Low, M.-M. & Klessen, R. S. 2004, *Reviews of modern physics*, 76, 125
- Maschberger, T., Clarke, C., Bonnell, I., & Kroupa, P. 2010, *Monthly Notices of the Royal Astronomical Society*, 404, 1061
- McKee, C. F. & Ostriker, E. C. 2007, *Annu. Rev. Astron. Astrophys.*, 45, 565
- McMillan, S., Portegies-Zwart, S., van Elteren, A., & Whitehead, A. 2012, *ADVANCES IN COMPUTATIONAL ASTROPHYSICS: METHODS, TOOLS AND OUTCOMES*, 453
- Parker, R. J. 2014, *Monthly Notices of the Royal Astronomical Society*, 445, 4037
- Parker, R. J. & Dale, J. E. 2015, *Monthly Notices of the Royal Astronomical Society*, 451, 3664
- Parker, R. J. & Meyer, M. R. 2012, *Monthly Notices of the Royal Astronomical Society*, 427, 637
- Parmentier, G. & Pfalzner, S. 2013, *Astronomy & Astrophysics*, 549, A132
- Pelupessy, F. I., Van Elteren, A., De Vries, N., et al. 2013, *Astronomy & Astrophysics*, 557, A84
- Portegies Zwart, S. & McMillan, S. 2018, *Astrophysical Recipes; The art of AMUSE*
- Portegies Zwart, S., van Elteren, A., Pelupessy, I., et al. 2019, *AMUSE: the Astrophysical Multipurpose Software Environment*
- Portegies Zwart, S. & Verbunt, F. 1996, *Astronomy and Astrophysics*, v. 309, p. 179-196, 309, 179
- Portegies Zwart, S. F., McMillan, S. L., & Gieles, M. 2010, *Annual review of astronomy and astrophysics*, 48, 431
- Qin, C., Pang, X., Pasquato, M., Kouwenhoven, M., & Vallenari, A. 2025, *Astronomy & Astrophysics*, 695, A22
- Sánchez, N. & Alfaro, E. J. 2009, *The Astrophysical Journal*, 696, 2086
- Sánchez, N., Alfaro, E. J., Elias, F., Delgado, A. J., & Cabrera-Cano, J. 2007, *The Astrophysical Journal*, 667, 213
- Schmeja, S. & Klessen, R. 2004, *Astronomy & Astrophysics*, 419, 405

- Schmeja, S. & Klessen, R. 2006, *Astronomy & Astrophysics*, 449, 151
- Shukirgaliyev, B., Otebay, A., Just, A., et al. 2019a, *Proceedings of the National Academy of Sciences of the Republic of Kazakhstan. Physical and Mathematical Series*, 130
- Shukirgaliyev, B., Otebay, A., Sobolenko, M., et al. 2021, *A&A*, 654, A53
- Shukirgaliyev, B., Parmentier, G., Berczik, P., & Just, A. 2017, *Astronomy & Astrophysics*, 605, A119
- Shukirgaliyev, B., Parmentier, G., Berczik, P., & Just, A. 2019b, *MNRAS*, 486, 1045
- Shukirgaliyev, B., Parmentier, G., Just, A., & Berczik, P. 2018, *ApJ*, 863, 171
- Sun, J., Gutermuth, R. A., Wang, H., Zhang, S., & Long, M. 2022, *Monthly Notices of the Royal Astronomical Society*, 516, 5258
- Toonen, S., Nelemans, G., & Zwart, S. P. 2012, *Astronomy & Astrophysics*, 546, A70
- Ussipov, N., Akhmetali, A., Zaidyn, M., et al. 2024, *Eurasian Physical Technical Journal*, 21
- Vázquez-Semadeni, E., González-Samaniego, A., & Colín, P. 2017, *Monthly Notices of the Royal Astronomical Society*, 467, 1313
- Wall, J. E., Mac Low, M.-M., McMillan, S. L., et al. 2020, *The Astrophysical Journal*, 904, 192
- Wall, J. E., McMillan, S. L., Mac Low, M.-M., Klessen, R. S., & Zwart, S. P. 2019, *The Astrophysical Journal*, 887, 62
- Weis, L., West, C., Just, A., et al. 2025, *A&A*, 703, A47
- Zwart, S. F. P., McMillan, S. L., van Elteren, A., Pelupessy, F. I., & de Vries, N. 2013, *Computer Physics Communications*, 184, 456
- Zwart, S. P., McMillan, S., Harfst, S., et al. 2009, *New Astronomy*, 14, 369
- Zwillinger, D. & Kokoska, S. 1999, *CRC standard probability and statistics tables and formulae* (Crc Press)

Appendix A: Simulations with no fractality

In this appendix, we present simulations that do not develop fractal structure during their evolution. As shown in Figure A.1, the Q parameter remains nearly constant throughout the simulation and stays in the regime associated with centrally concentrated stellar distributions. This indicates that the stellar distribution does not fragment into subclusters; instead, the systems evolve into centrally concentrated clusters while preserving a largely smooth global spatial distribution.

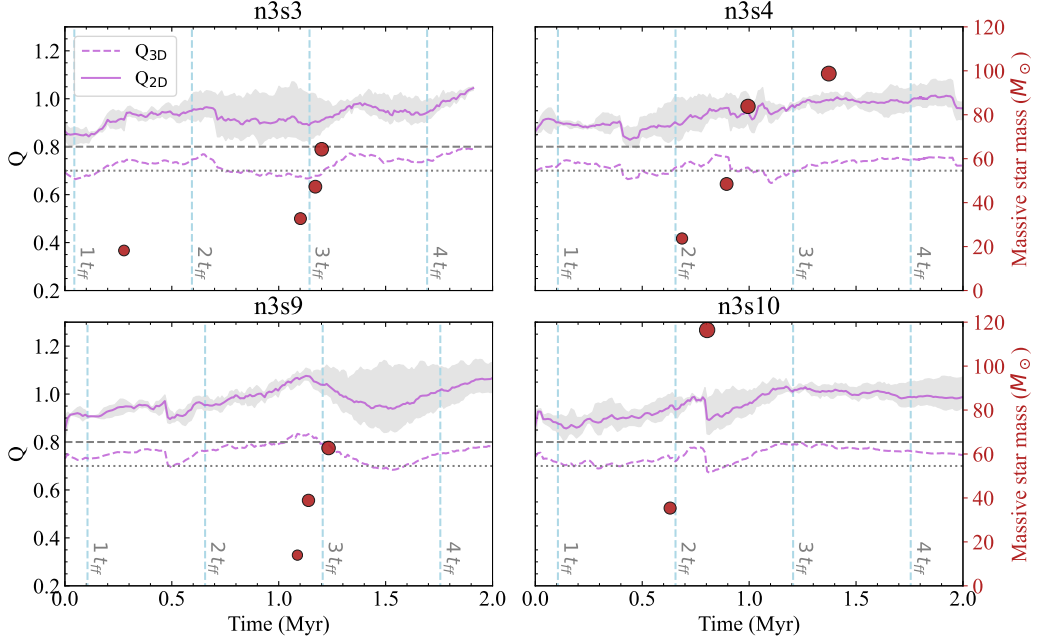


Fig. A.1: Evolution of the Q parameter over time in models that initially show no fractality. All notations are the same as in Figure 3.

The corresponding evolution of the fractal dimension f_{dim} is shown in Figure A.2. Overall, these models exhibit values of f_{dim} similar to those discussed in the main text. However, in contrast to simulations that develop fractal substructure, the fractal dimension in these models tends to plateau at slightly lower values.

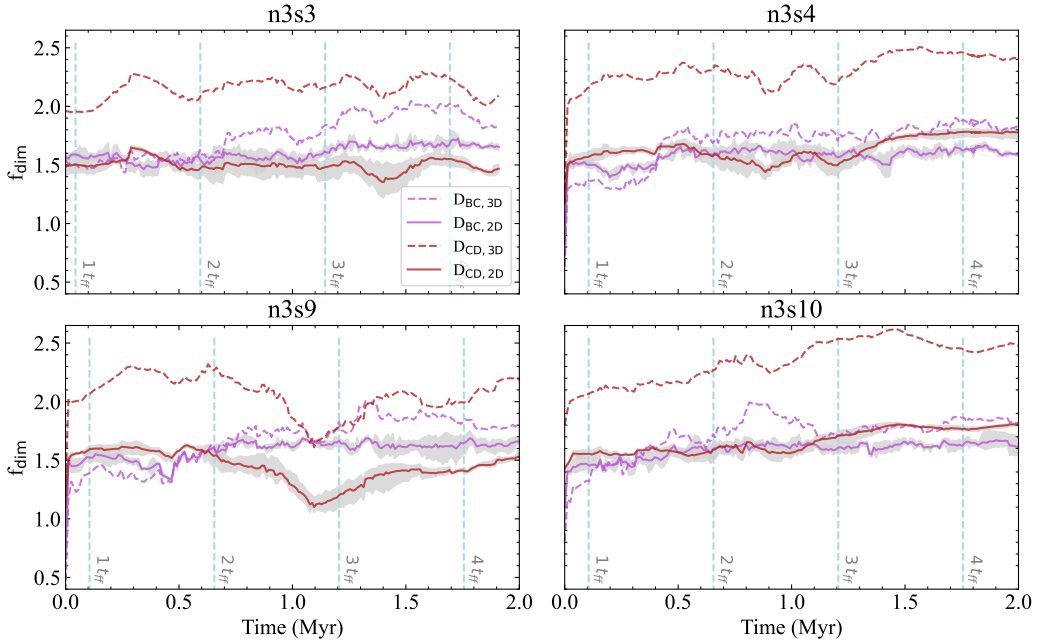


Fig. A.2: Evolution of the fractal dimension f_{dim} over time in models that initially show no fractality, for comparison with Figure A.1. All notations are the same as in Figure 6.